Enhanced hot-electron production and strong-shock generation in hydrogen-rich ablators for shock ignition

W. Theobald, A. Bose, R. Yan, R. Betti, M. Lafon, D. Mangino, A. R Christopherson, C. Stoeckl, W. Seka, W. Shang, et al.

Enhanced Hot-Electron Production and Strong-Shock Generation in Hydrogen-Rich Ablators for Shock Ignition

W. Theobald[1,2,*] A. Bose[1,2,3], R. Yan[4,5], R. Betti[1,2,3,4], M. Lafon[1,6], D. Mangino[4], A. R. Christopherson[1,2,4], C. Stoeckl[1], W. Seka[1], W. Shang[1,2,†] D. T. Michel[1], C. Ren[1,3,4], R. C. Nora[7], A. Casner[6,8], J. Peebles[1], F. N. Beg[9], X. Ribeyre[8], E. Llor Aisa[8], A. Colaïtis[8], V. Tikhonchuk[8], and M. S. Wei[10]

[1]*Laboratory for Laser Energetics, University of Rochester, Rochester, NY*
[2]*Fusion Science Center, University of Rochester, Rochester, NY*
[3]*Department of Physics and Astronomy, University of Rochester, Rochester, NY*
[4]*Department of Mechanical Engineering, University of Rochester, Rochester, NY*
[5]*Department of Modern Mechanics, University of Science and Technology of China, Hefei, Peoples Republic of China*
[6]*CEA, DAM, DIF, F-91297 Arpajon, France*
[7]*Lawrence Livermore National Laboratory, Livermore, CA*
[8]*Centre Lasers Intenses et Applications, CELIA, Université Bordeaux CEA-CNRS, Talence, France*
[9]*University of California-San Diego, La Jolla, CA and*
[10]*General Atomics, San Diego, CA, USA*

(Dated: October 31, 2017)

Experiments were performed with CH, Be, C, and SiO_2 ablators interacting with high-intensity UV laser radiation (5×10^{15} W/cm^2, λ = 351 nm) to determine the optimum material for hot-electron production and strong-shock generation. Significantly more hot electrons are produced in CH (up to ∼13% instantaneous conversion efficiency), while the amount is a factor of ∼2 to 3 lower in the other ablators. A larger hot-electron fraction is correlated with a higher effective ablation pressure. The higher conversion efficiency in CH is attributed to stronger damping of ion-acoustic waves because of the presence of light H ions.

Generating strong shocks up to several hundred megabars allows one to explore plasma and material properties at the most-extreme conditions of energy density. It also enables one to develop two-step inertial confinement fusion (ICF) schemes, where ignition is separated from the main compression of the thermonuclear fuel. A promising two-step ignition scheme is shock ignition (SI) [1–4], where ignition is triggered by a strong shock launched at the end of the implosion and driven by a pressure above ∼300 Mbar. Detailed reviews of the current status and physics issues for SI are found in Refs. [5–7]. One of the most critical issues is the high UV laser intensity of 5×10^{15} to 1×10^{16} W/cm^2 required by the ignitor spike pulse. The spike will excite parametric laser–plasma instabilities (LPI's) in the hot plasma corona surrounding the imploding capsule, thereby transferring a significant amount of laser energy to hot electrons. Recent work [8–10] demonstrated that hot electrons can enhance the shock pressure. It is still an open question whether they might preheat a SI target [11] or if the benefits prevail because the areal density is large enough to stop them in the shell and augment the shock strength [12, 13]. Another concern pertains to the energy coupling. The spike pulse must couple sufficient energy to the target in order to generate a strong-enough shock. LPI's may reduce the coupling efficiency and prevent the seed shock pressure from reaching the required magnitude.

Directly measuring the pressure at these high intensities is nearly impossible, so it must be instead inferred indirectly. Experiments in planar geometry at the LULI [14], Omega [15], and PALS [16] Laser Facilities have inferred ablation pressures in the range of ∼40 to 90 Mbar, which were limited by lateral heat flow from the laser spots in the planar geometries. The lateral transport was suppressed with the development of a new platform [17, 18] that applies spherical targets and x-ray diagnostics. It allows one to evaluate the pressure at SI–relevant laser intensities. The laser launches into the solid target an inwardly propagating shock wave that converges at the center, generating a short x-ray flash that is measured with a time-resolved diagnostic. Several experiments established this scheme as a reliable platform using a variety of laser energies, pulse shapes, and target diameters [18].

There is a continuing interest in exploring new ablator materials in direct-drive ICF research in order to improve the hydrodynamic efficiency [19], mitigate the hot-electron production [20, 21], and suppress the Rayleigh–Taylor instability [22–24]. Recent theoretical work demonstrated an overall better performance with mid-Z ablators than plastic (CH) by suppressing the threshold of detrimental LPI while preserving the hydrodynamic stability properties [25]. All of this work has been performed, however, at low laser intensities of up to $\sim1\times10^{15}$ W/cm^2, which is relevant for the standard hot-spot–ignition concept but not for the spike interaction in SI.

This Letter describes for the first time that the ablator plays an important role at SI–relevant laser intensities. The experiment shows that CH produces significantly more hot electrons and stronger shocks than the

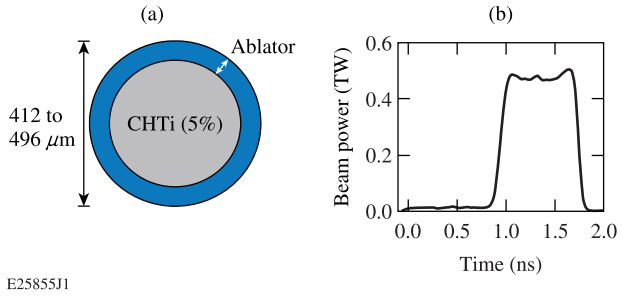

FIG. 1. (a) Target design consisting of an outer ablator layer of various materials and an inner Ti-doped plastic core; (b) pulse shape.

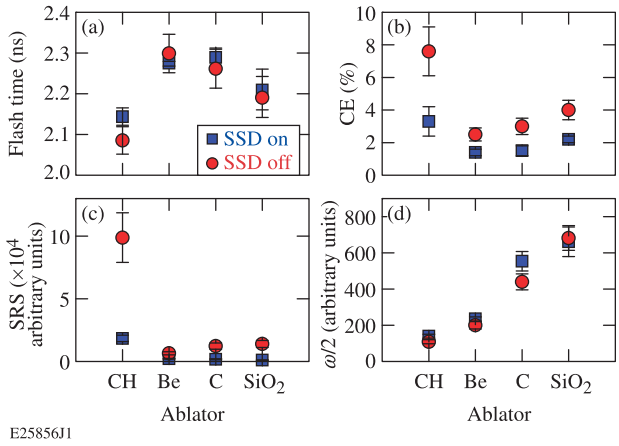

FIG. 2. (a) X-ray flash time for different ablators with smoothing by spectral dispersion (SSD) on (squares) and SSD off (circles); (b) measured time-integrated conversion efficiency (CE) of laser energy into hot-electron energy; (c) stimulated Raman scattering (SRS) backscatter signal, and (d) $\omega/2$ signal.

other materials. This important finding sheds light on the laser plasma–interaction physics in an intensity and plasma regime, which is insufficiently explored and might provide a path to higher energy density states in direct-drive geometry.

The experiment used 60 UV ($\lambda = 351$ nm) beams from the OMEGA laser [26] with a total energy of 22 to 26 kJ that were focused to an overlapping intensity of up to $\sim 5\times10^{15}$ W/cm^2 on the surface of a spherical solid target. The beams were equipped with small-spot phase plates [27], polarization smoothing [28], and smoothing by spectral dispersion (SSD) [29]. The single-beam intensity was $\sim 4\times10^{14}$ W/cm^2 for SSD on and $\sim 6\times10^{14}$ W/cm^2 for SSD off. The targets with an outer diameter (OD) of 412 to 496 μm consisted of an inner CH core that was doped with Ti with an atomic concentration of 5% and an outer ablator layer with a thickness (t) of 20 to 46 μm of a different material [Fig. 1(a)]. The outer layer was irradiated with the laser pulse shown in Fig. 1(b). A low-power prepulse of ~1-ns duration produced a plasma corona with which the high-power part of the pulse interacted to generate the shock and the hot electrons. Four ablators (CH, Be, C, and SiO_2) with different atomic numbers (Z) were used. Table I summarizes the parameters. The shock wave collapsed in the center, resulting in a short burst of x-ray radiation that was detected spatially and temporally resolved with multiple x-ray framing cameras. Each framing camera was absolutely timed through dedicated timing shots [19, 30] with an accuracy of 30 ps. Time-resolved and time-integrated hard x-ray measurements provide a characterization of the hot-electron population (hot-electron temperature and total energy). Details on this can be found in Ref. [18] and references therein. The output from a radiation–hydrodynamics simulation for each target was used as an input for a Monte Carlo electron and photon transport code simulation (ITS 3.0) to calculate the bremsstrahlung emission for each diagnostic channel and compare it to the measurement. The hot-electron energy and temperature were varied until good agreement between calculations and experimental values were achieved. The instrument response function was also modeled with the Monte Carlo code. The Monte Carlo simulation takes the material effects into account and calculates the hot-electron stopping in the compressed target and the resulting hard x-ray emission including opacity effects. Optical backscatter diagnostics measured the amount of backscattered energy at the laser wavelength and provided temporally streaked spectra of the stimulated Brillouin scattering (SBS) and the stimulated Raman scattering (SRS). A quantity α is defined as $\alpha = 1 - E_{351}/E_L$, where E_{351} is the measured backscattered energy around the laser wavelength and E_L is the measured incident laser energy.

Figure 2(a) shows the measured flash time, which is defined as the occurrence of the x-ray flash relative to the start of the laser pulse, for the different ablators with SSD on (squares) and SSD off (circles) in sequence of increasing Z. The measured flash times were adjusted to account for differences in target size, laser energy, and t. One-dimensional (1-D) radiation–hydrodynamics simulations were performed with the code *LILAC* [33] to analyze the dependence of the flash time on the different variables for each material. The flash times were then adjusted for an ablator thickness that resulted in a constant ablator mass of 20.8 μg, a laser energy of 24 kJ, and a diameter of 372 μm for the Ti doped CH part of the target to obtain a valid comparison for the different targets. The timing adjustments were between 43 ps and 10 ps for CH and smaller than 64 ps for the other materials. The data show the general trend of an earlier flash with increasing Z except for CH, which produced the earliest flash. Turning SSD off advances the flash in CH by ~70 ps while no significant effect is observed in the other materials. Figure 2(b) shows the measured time-

Ablator	OD (μm)	t (μm)	ρ (g/cm^3)	T_e (keV)	T_i (keV)	R (μm)	L (μm)	I_{TPD} (W/cm^2)	I_{SRS} (W/cm^2)
CH	454	40	1.04 ± 0.01	3.6	0.7	310	125	7×10^{14}	3×10^{14}
Be	430	20	1.84 ± 0.01	3.7	0.5	302	110	8×10^{14}	3×10^{14}
C	444	28	1.4 ± 0.4	4.0	0.7	288	125	7×10^{14}	3×10^{14}
SiO_2	433	20	1.75 ± 0.2	4.2	0.9	302	115	9×10^{14}	3×10^{14}

TABLE I. Ablators along with the average outer target diameter (OD), average layer thickness (t), and measured mass density (ρ). Also given are calculated plasma parameters at the quarter-critical density ($n_c/4$) of electron temperature (T_e), ion temperature (T_i), radial position of $n_c/4$ (R), and density scale length (L) from radiation–hydrodynamics simulations. The last two columns list calculated intensity thresholds for the two-plasmon decay (TPD) [31] and stimulated Raman backscatter (SRS) [32] instabilities.

integrated conversion efficiency (CE). Plastic stands out by producing by far the most hot-electrons with up to ∼2 kJ of total hot-electron energy (time-integrated CE ∼8%) when SSD was turned off. Nine and seven shots were performed for CH with SSD on and off, respectively, to prove that the observed difference is not an artifact. If CH is treated as an exception, there is the general trend of a slight increase in hot-electron production with higher Z. The inferred hot-electron temperatures lie between 60 and 80 keV and are independent of the ablator and SSD. A higher hot-electron fraction corresponds to an earlier flash time, which indicates that hot electrons play a role in the shock formation and augment its strength. The experimental data provide information about the mechanism of hot-electron generation. A clear correlation between hot-electron production and the SRS backscatter signal is observed [Fig. 2(c)]. Switching SSD on significantly decreases the SRS signal in all ablators, potentially the result of the suppression of beam filamentation. The detected SRS wavelengths range from ∼560 to ∼680 nm, indicating that SRS is produced in a plasma region between 0.07 n_e/n_c and 0.20 n_e/n_c, where n_e is the electron density and n_c is the critical density for 351-nm light. No absolute measurement of the SRS backscatter was available for these shots because of a calibration issue with the diagnostic. The weaker optical emission generated by electron plasma waves (EPW's) with half the laser frequency ($\omega/2$) increases monotonically with Z [Fig. 2(d)].

The quantity α was measured for the different ablators. CH produced the highest α [0.62±0.04 (SSD on), 0.71±0.03 (SSD off)] followed by SiO_2 [0.60±0.04 (SSD on), 0.61±0.04 (SSD off)], C [0.60±0.04 (SSD on), 0.63±0.04 (SSD off)], and Be [0.56±0.04 for both]. Energy conservation requires that $E_L = E_{abs} + E_{351} + E_{SRS} + E_h$, where E_{abs} is the absorbed energy in the plasma, E_{SRS} is the SRS backscattered energy, and E_h is the hot electron energy. E_{SRS} was not measured, but one can argue that it msut be roughly equal to E_h. Assuming $E_{SRS} = E_h$, the absorbed energy is $E_{abs} \approx E_L - E_{351} - 2E_h = (\alpha - 2CE)E_L$. Using, e.g., the measured values for CH and SSD off, the absorbed energy is $E_{abs}^{CH,off} \approx 0.56E_L$. A very similar value of $E_{abs}^{CH,on} \approx 0.55E_L$ is obtained for SSD on, showing that only about half of the laser energy is absorbed in the plasma. Similar values are obtained for the other materials. The high value of α for CH and SSD off is a result of the large amount of SRS backscattering and hot electron energy. Therefor, absorption is about equal in all the materials and for SSD on and off. The absorbed energy fractions from simulations are in the range of ∼40% to 60% and are consistent with the experimental values within the error. Since only ∼5% of the absorbed energy is coupled to the hydrodynamic drive it is reasonable to conclude that small discrepancies between simulated and experimentally-inferred laser absorptions are negligible compared to the large effects of hot electron energy deposition when it comes to producing higher pressures in the target. The variation in flash time can therefore not be explained by a difference in absorbed energy but is likely the consequence of a difference in E_h.

An effective maximum ablation pressure has been inferred [see Fig. 3(a)] from *LILAC* simulations. The effect of hot electrons was taken into account by increasing the flux limiter [34] so that the flash time was recovered in the simulations for each ablator material. Although it has been shown in Ref. [17] that the pressure increase from hot electrons may be described by an increased flux limiter, this simplified description does not capture important details such as slowing down, preheat, and local energy deposition. Therefore, additional simulations were performed for CH and C that included a detailed hot-electron transport model, which confirmed the pressures shown in Fig. 3(a). The simulation details are discussed in Ref. [17]. Briefly, the measured hot-electron fraction and temperature were used as input in the *LILAC* simulations as well as the temporal dependence of the hot-electron production. The simulations employed a multigroup radiation diffusion model, an equation-of-state model based on SESAME tables, flux-limited thermal transport, and a hot-electron transport package. A fraction of the laser energy reaching the quarter-critical surface is converted into hot electrons, assuming a single-temperature Maxwellian distribution and an isotropic emission within a 120° full divergence angle in the forward direction. The hot electrons are transported in straight lines into the target. The simulations show that the hot electrons increase the effective

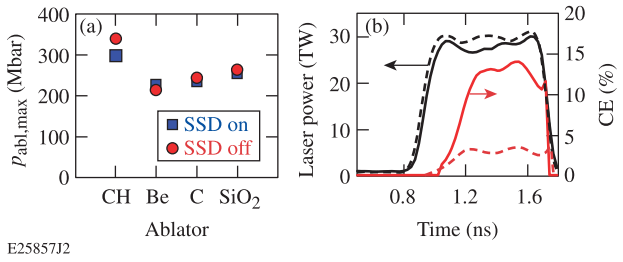

FIG. 3. (a) Inferred effective maximum ablation pressures for the various materials for an incident laser intensity of 5×10^{15} W/cm^2. (b) Inferred time-resolved CE (red) and laser pulse shapes (black) for two shots with CH (solid curves, shot 73648) and C (dashed curves, shot 73645). Both shots were taken with SSD off. The time resolution of CE is ∼100 ps.

maximum ablation pressure in CH by 77% and in C by 45%.

Figure 3(b) shows the inferred time-resolved CE (red) for two shots with CH (solid) and C (dashed). The black curves represent the corresponding laser pulse shapes. The onset of hot-electron production lags by ∼0.2 ns with respect to the rising edge of the laser pulse. This is explained by a strong SBS backscatter spike with a width of ∼0.2 ns upon the arrival of the main pulse, which reduces temporarily the laser intensity around $n_c/4$ below the thresholds of the SRS and two-plasmon–decay (TPD) instabilities. In addition, the change in temperature and density scale length in this region also directly affects the LPI thresholds. *LILAC* simulations show that a plateau in the velocity profile develops in the region between $n_c/10$ and $n_c/4$, which promotes a high SBS gain during this time. Averaged over the laser pulse shape and over the full target sphere, SBS scatters back $\sim 2-3\%$ of the laser energy for CH, while this fraction is below 2% for the other ablators. A comparison of the simulations of the two shots shown in Fig. 3(b) reveals that at the time of the observed SBS spike, there is a difference in the flow velocity gradient of both materials. The velocity profile for CH is much shallower than for C. This probably caused a higher SBS gain in CH than in C. Time-resolved measurements of the SRS backscattering appear closely correlated with the hot-electron production. The time-resolved CE is based on the measured time-resolved hard x-ray emission [35] in the photon energy range between 50 and 100 keV. It is assumed that the instantaneous amount of hot electrons is proportional to the instantaneous hard x-ray emission and that the time-integrated CE equals the measured time-integrated values [see Fig. 2(b)]. The CE reached 13±2% and 4±1% in CH and C, respectively, during the second half of the high-intensity pulse, while the time-integrated CE over the entire pulse, including the laser energy when no hot electrons were generated, yielded 9±1% and 3±1%, respectively, for these shots.

Plasma parameters such as the electron temperature (T_e) and the density scale length (L) play an important role in the development of LPI. Table I provides the relevant coronal plasma parameters from *LILAC* simulations of the different materials at the $n_c/4$ position and the calculated threshold intensities for TPD and SRS. Slight differences in the plasma parameters and the calculated threshold intensities are observed between materials. First, threshold intensities for SRS are about a factor of 2 lower than for TPD for all materials, which explains why SRS is the dominant hot-electron production mechanism at these high T_e's. Second, SRS thresholds are the same, which suggests that from a hydrodynamic point of view, no difference in hot-electron production for different materials is expected. This is in contrast to the experiment and points to a different cause. Coronal conditions of a full-scale SI target have been calculated at the $n_c/4$ point for a polar-driven shock-ignition design for the National Ignition Facility [13]. At the peak of the laser spike values of $T_e = 8.5$ keV and $L = 450$ um were calculated, which show that in the OMEGA experiment the temperatures are a factor of ∼2 lower and L is a factor of ∼4 shorter compared to an ignition target.

Cross-beam energy transfer (CBET) can limit the ablation pressure in direct-drive implosions. CBET depends on such parameters as the laser spot size relative to the target size, the spectrum of the laser beams, and the damping of ion-acoustic waves (IAW's). Experiments with imploding thin CH shells on OMEGA at an intensity of 5×10^{14} W/cm^2 studied the effect of the beam size for ratios of laser-spot radius to target radius from $R = 1.1$ to 0.5 (Ref. [36]). The experiments reported here employed solid targets with $R = 1$ for SSD on and $R = 0.85$ for SSD off, assuming an average of the major and minor axes of the elliptical focus profiles and a standard target radius of 215 μm. Based on the smaller ratio for SSD off, we would expect a reduction in CBET and a corresponding increase in hydrodynamic efficiency. The experiments indicate that the variation in beam size due to SSD does not play a role. With the exception of CH, which has the highest hot-electron production, the flash time [see Fig. 2(a)] is not influenced by SSD. SSD increased the spectral bandwidth to ∼1 Å. Previous experiments and simulations indicate that this width is not sufficient to affect CBET [37]. The damping rates are significantly higher in CH than in C (see below); therefore CBET should be less effective in CH. Although it cannot be ruled out that CBET mitigation does play a role in CH, the increased coupled drive energy in CH is believed to be mainly the result of an increased coupling of hot electrons. It has been demonstrated in Ref. [17] that hot electrons with a total energy of ∼2 kJ play an important role in the shock formation in these experiments. Note that the total internal and kinetic energy supplied to the imploding target is ∼0.6 kJ (∼5% hydroefficiency). Therefore ∼2 kJ of hot-electron energy is sufficient to significantly affect the target dynamics.

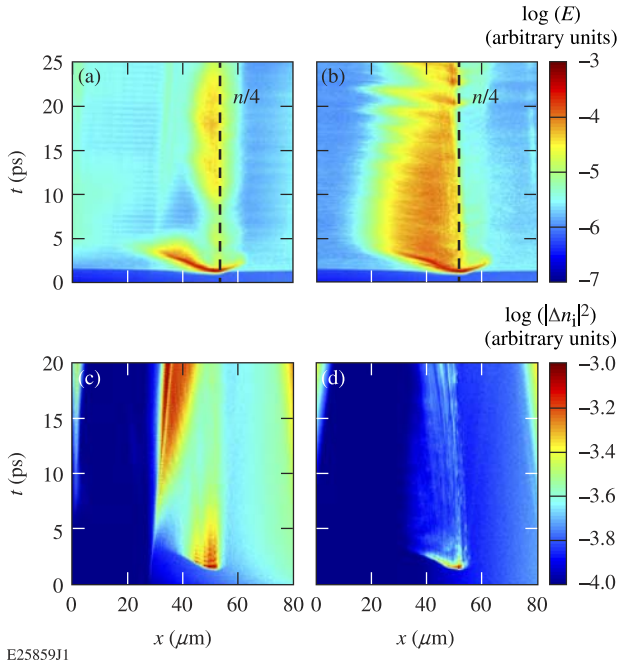

FIG. 4. Calculated longitudinal electric-field strength versus time and space (laser propagates from left to right) for (a) C and (b) CH and calculated ion-acoustic wave level for (c) C and (d) CH. The quantities were averaged over the transversal space coordinate and rendered on a logarithmic scale. The C simulation used a CH layer in the underdense portion, and the pure C layer starts at $x = 30$ μm.

The experiments demonstrate significant differences between CH and C, indicating that the H species plays an important role in the LPI. Other experiments that are relevant for indirect drive using low-density ($n_e/n_c \sim 0.1$), high-Z Xe plasmas that were doped with low-Z impurity (C_5H_{12}) have demonstrated an enhanced SRS reflectivity with higher impurity concentration [38, 39]. The increased SRS reflectivity has been linked to an increased damping of IAW's, which is especially high for plasmas containing H [40]; however, no hot-electron measurements were reported [38–40]. To elucidate the SRS physics of this experiment, 2-D particle-in-cell (PIC) simulations were performed using the code *OSIRIS* [41] by comparing simulations with and without H in the vicinity of $n_c/4$. A simulation with CH was compared to one where H was removed in the vicinity of $n_c/4$ ($n_e > 0.2$ n_c). These simulations were designed to identify differences in the fundamental physics of SRS caused by the presence of H. A boundary with matched density between CH in the underdense region and pure C in the higher-density region ensured that equal conditions are created for the laser pulse propagating through the underdense plasma. The input parameters were obtained from a radiation–hydrodynamics simulation for a CH shot evaluated at 1.5 ns, when peak hot-electron production was observed. The PIC simulations assumed the same initial plasma parameters. The input thermal electron and ion temperatures were $T_e = 4$ keV and $T_i = 0.8$ keV, respectively, and the plasma density ramped linearly from 0.12 n_c to 0.30 n_c with $L = 123$ μm. A plane-wave ($\lambda = 351$ nm) laser pulse propagated along the x axis with a nominal intensity of 2.6×10^{15} W/cm^2 (the same intensity as at $n_c/4$ in the implosion), assuming flattop profiles in both time and space. The effect of SSD was not taken into account in the simulation.

Figures 4(a) and 4(b) show the calculated longitudinal electric-field strength from EPW versus time and laser propagation direction for C and CH, respectively. Distinct differences in the fields are observed. The electromagnetic wave excites strong EPW over a large region in CH compared to C. The wave modes survive longer in CH and couple better with thermal electrons because of a larger **k** vector. Determined by the phase-matching condition and the dispersion relations, the EPW's at the lower-density region have larger **k**. These large-**k** modes can accelerate thermal electrons more efficiently since their phase velocity is closer to the electron thermal velocity than the small-**k** modes close to $n_c/4$ (Ref. [42]). Figures 4(c) and 4(d) compare the calculated signal level of IAW's, showing a stronger damping in CH compared to C because of the presence of light H ions. The Landau damping rates [43] were calculated for plasma conditions $T_e = 4$ keV, $T_i = 0.8$ keV, k=$2k_0$ for CH and C, where k and k_0 are the absolute values of the IAW and the laser wave vectors. At $0.25n_c$, $\gamma = 7.4\times10^{-4}\omega_0$ (CH) and $\gamma = 2.2\times10^{-5}\omega_0$ (C), where ω_0 is the laser frequency, while for a lower density of $0.12n_c$ the calculations yield $\gamma = 5.8\times10^{-4}\omega_0$ (CH) and $\gamma = 1.9\times10^{-5}\omega_0$ (C). Damping from ion–electron collisions is negligible. This shows that the IAW damping rate in CH is ~30× of that in C. The calculated CE's from the PIC simulations were 12% and 2% for CH and C, respectively, accounting for electrons with kinetic energy > 50 keV. A likely explanation is that the SRS saturation level is controlled by the secondary parametric decay of the driven EPW or its collapse, similar to the observations reported in Refs. [38, 39]. The secondary parametric decay has been discussed in many papers; the experimental demonstration was reported in Ref. [44]. The threshold of the parametric decay is proportional to the IAW damping rate. In the case of a high IAW damping (with H), the threshold is higher and the EPW amplitude can grow to higher level, producing a stronger SRS signal and a larger number of hot electrons.

In conclusion, experiments were performed with CH, Be, C, and SiO_2 ablators at SI-relevant laser intensities. We observed peculiar differences in the hot-electron production and the shock formation and found that CH produced the largest amount of hot electrons and the strongest shocks. Supporting PIC simulations show that the strong damping of IAW's in the CH plasma causes an increased growth of EPWs and hot-electron produc-

tion. In contrast to other work [19], which showed that Be ablators are the preferred choice at much lower laser intensity in a regime that is applicable to the standard hot-spot–ignition scheme, we found that among the four investigated materials, Be is the least efficient for SI since it produced the lowest effective ablation pressure inferred from shock velocities at the incident laser intensity of 5×10^{15} W/cm^2. The results demonstrate that the ablator material plays an important role in the energy coupling of the spike pulse and must be carefully considered in the design of ignition-relevant targets.

This work was supported by the DOE NNSA under awards No. DE-NA0001944 and DE-FC02-04ER54789, the Laboratory Basic Science Program, the University of Rochester, and the New York State Energy Research and Development Authority. We acknowledge the *OSIRIS* Consortium for the use of *OSIRIS*. R.Y. acknowledges support by the Science Challenge Project of China (No. JCKY2016212A501, No. JCKY2016212A505). Part of this work has been carried out within the framework of the EUROfusion Consortium and has received funding from the European Union's Horizon 2020 research and innovation program under grant agreement No. 633053.

* wthe@lle.rochester.edu
† On leave from Research Center of Laser Fusion, China Academy of Engineering Physics, Mianyang, Peoples Republic of China

[1] R. Betti, C. D. Zhou, K. S. Anderson, L. J. Perkins, W. Theobald, and A. A. Solodov, Phys. Rev. Lett. **98**, 155001 (2007).
[2] W. Theobald, R. Betti, C. Stoeckl, K. S. Anderson, J. A. Delettrez, V. Yu. Glebov, V. N. Goncharov, F. J. Marshall, D. N. Maywar, R. L. McCrory, D. D. Meyerhofer, P. B. Radha, T. C. Sangster, W. Seka, D. Shvarts, V. A. Smalyuk, A. A. Solodov, B. Yaakobi, C. D. Zhou, J. A. Frenje, C. K. Li, F. H. Sguin, R. D. Petrasso, and L. J. Perkins, Phys. Plasmas **15**, 056306 (2008).
[3] X. Ribeyre, G. Schurtz, M. Lafon, S. Galera, and S. Weber, Plasma Phys. Controlled Fusion **51**, 015013 (2009).
[4] L. J. Perkins, R. Betti, K. N. LaFortune, and W. H. Williams, Phys. Rev. Lett. **103**, 045004 (2009).
[5] S. Atzeni, X. Ribeyre, G. Schurtz, A. J. Schmitt, B. Canaud, R. Betti, and L. J. Perkins, Nucl. Fusion **54**, 054008 (2014).
[6] D. Batani, S. Baton, A. Casner, S. Depierreux, M. Hohenberger, O. Klimo, M. Koenig, C. Labaune, X. Ribeyre, C. Rousseaux, W. Theobald, and V. T. Tikhonchuk, Nucl. Fusion **54**, 054009 (2014).
[7] R. Betti and O. Hurricane, Nature Physics **12**, 435 (2016).
[8] S. Yu. Guskov, X. Ribeyre, M. Touati, J. L. Feugeas, Ph. Nicolai, and V. Tikhonchuk, Phys. Rev. Lett. **109**, 255004 (2012); X. Ribeyre, S. Guskov, J. L. Feugeas, Ph. Nicolai, and V. T. Tikhonchuk, Phys. Plasmas **20**, 062705 (2013).
[9] E. Llor Aisa, X. Ribeyre, S. Guskov, Ph. Nicola, and V. T. Tikhonchuk, Phys. Plasmas **22**, 102704 (2015).
[10] Ph. Nicolai, J.-L. Feugeas, T. Nguyen-bui, V. Tikhonchuk, L. Antonelli, D. Batani, and Y. Maheut, Phys. Plasmas **22**, 042705 (2015).
[11] A. Colaïtis, X. Ribeyre, E. Le Bel, G. Duchateau, Ph. Nicolam, and V. Tikhonchuk, Phys. Plasmas **23**, 072703 (2016).
[12] R. Betti, W. Theobald, C. D. Zhou, K. S. Anderson, P. W. McKenty, S. Skupsky, D. Shvarts, V. N. Goncharov, J. A. Delettrez, P. B. Radha, T. C. Sangster, C. Stoeckl, and D. D. Meyerhofer, J. Phys. Conf. Ser. **112**, 022024 (2008).
[13] K. S. Anderson, K. S. Anderson, R. Betti, P. W. McKenty, T. J. B. Collins, M. Hohenberger, W. Theobald, R. S. Craxton, J. A. Delettrez, M. Lafon, J. A. Marozas, R. Nora, S. Skupsky, and A. Shvydky, Phys. Plasmas **20**, 056312 (2013).
[14] S. D. Baton, M. Koenig, E. Brambrink, H. P. Schlenvoigt, C. Rousseaux, G. Debras, S. Laffite, P. Loiseau, F. Philippe, X. Ribeyre, and G. Schurtz, Phys. Rev. Lett. **108**, 195002 (2012).
[15] M. Hohenberger, W. Theobald, S. X. Hu, K. S. Anderson, R. Betti, T. R. Boehly, A. Casner, D. E. Fratanduono, M. Lafon, D. D. Meyerhofer, R. Nora, X. Ribeyre, T. C. Sangster, G. Schurtz, W. Seka, C. Stoeckl, and B. Yaakobi, Phys. Plasmas **21**, 022702 (2014).
[16] D. Batani, L. Antonelli, S. Atzeni, J. Badziak, F. Baffigi, T. Chodukowski, F. Consoli, G. Cristoforetti, R. De Angelis, R. Dudzak, , G. Folpini, L. Giuffrida, L. A. Gizzi, Z. Kalinowska, P. Koester, E. Krousky, M. Krus, L. Labate, T. Levato, Y. Maheut, G. Malka, D. Margarone, A. Marocchino, J. Nejdl, Ph. Nicolai, T. ODell, T. Pisarczyk, O. Renner, Y. J. Rhee, X. Ribeyre, M. Richetta, M. Rosinski, M. Sawicka, A. Schiavi, J. Skala, M. Smid, Ch. Spindloe, J. Ullschmied, A. Velyhan, and T. Vinci, Phys. Plasmas **21**, 032710 (2014).
[17] R. Nora, W. Theobald, R. Betti, F. J. Marshall, D. T. Michel, W. Seka, B. Yaakobi, M. Lafon, C. Stoeckl, J. A. Delettrez, A. A. Solodov, A. Casner, C. Reverdin, X. Ribeyre, A. Vallet, J. Peebles, F. N. Beg, M. S. Wei, and R. Betti, Phys. Rev. Lett. **114**, 045001 (2015).
[18] W. Theobald, R. Nora, W. Seka, M. Lafon, K. S. Anderson, M. Hohenberger, F. J. Marshall, D. T. Michel, A. A. Solodov, C. Stoeckl, D. Edgell, B. Yaakobi, A. Casner, C. Reverdin, X. Ribeyre, O. Shvydky, A. Vallet, J. Peebles, F. N. Beg, M. S. Wei, and R. Betti, Phys. Plasmas **22**,

056310 (2015).
[19] D. T. Michel, V. N. Goncharov, I. V. Igumenshchev, R. Epstein, and D. H. Froula, Phys. Rev. Lett. **111**, 245005 (2013).
[20] J. F. Myatt, H. X. Vu, D. F. DuBois, D. A. Russell, J. Zhang, R. W. Short, and A. V. Maximov, Phys. Plasmas **20**, 052705 (2013).
[21] S. X. Hu, D. T. Michel, D. H. Edgell, D. H. Froula, R. K. Follett, V. N. Goncharov, J. F. Myatt, S. Skupsky, and B. Yaakobi, Phys. Plasmas **20**, 032704 (2013).
[22] S. Fujioka, A. Sunahara, N. Ohnishi, Y. Tamari, K. Nishihara, H. Azechi, H. Shiraga, M. Nakai, K. Shigemori, T. Sakaiya, M. Tanaka, K. Otani, K. Okuno, T. Watari, T. Yamada, M. Murakami, K. Nagai, T. Norimatsu, Y. Izawa, S. Nozaki, and Y. Chen, Phys. Plasmas **11**, 2814 (2004).
[23] A. N. Mostovych, D. G. Colombant, M. Karasik, J. P. Knauer, A. J. Schmitt, and J. L. Weaver, Phys. Rev. Lett. **100**, 075002 (2008).
[24] G. Fiksel, S. X. Hu, V. N. Goncharov, D. D. Meyerhofer, T. C. Sangster, V. A. Smalyuk, B. Yaakobi, M. J. Bonino, and R. Jungquist, Phys. Plasmas **19**, 062704 (2012).
[25] M. Lafon, R. Betti, K. S. Anderson, T. J. B. Collins, R. Epstein, P. W. McKenty, J. F. Myatt, A. Shvydky, and S. Skupsky, Phys. Plasmas **22**, 032703 (2015).
[26] T. R. Boehly, D. L. Brown, R. S. Craxton, R. L. Keck, J. P. Knauer, J. H. Kelly, T. J. Kessler, S. A. Kumpan, S. J. Loucks, S. A. Letzring, F. J. Marshall, R. L. McCrory, S. F. B. Morse, W. Seka, J. M. Soures, and C. P. Verdon, Opt. Commun. **133**, 495 (1997).
[27] S. P. Regan, T. C. Sangster, D. D. Meyerhofer, W. Seka, R. Epstein, S. J. Loucks, R. L. McCrory, C. Stoeckl, V. Yu. Glebov, O. S. Jones, D. A. Callahan, P. A. Amendt, N. B. Meezan, L. J. Suter, M. D. Rosen, O. L. Landen, E. L. DeWald, S. H. Glenzer, C. Sorce, S. Dixit, R. E. Turner, and B. MacGowan, J. Phys.: Conf. Ser. **112**, 022077 (2008).
[28] T. R. Boehly, V. A. Smalyuk, D. D. Meyerhofer, J. P. Knauer, D. K. Bradley, R. S. Craxton, M. J. Guardalben, S. Skupsky, and T. J. Kessler, J. Appl. Phys. **85**, 3444 (1999).
[29] S. Skupsky, R. W. Short, T. Kessler, R. S. Craxton, S. Letzring, and J. W. Soures, J. Appl. Phys. **66**, 3456 (1989).
[30] D. T. Michel, A. K. Davis, W. Armstrong, R. Bahr, R. Epstein, V. N. Goncharov, M. Hohenberger, I. V. Igumenshchev, R. Jungquist, D. D. Meyerhofer, P.B. Radha, T.C. Sangster, C. Sorce, and D.H. Froula, High Power Laser Science and Engineering **3**, e19 (2015).
[31] A. Simon, R. W. Short, E. A. Williams, and T. Dewandre, Phys. Fluids **26**, 3107 (1983).
[32] C. S. Liu, Marshall N. Rosenbluth, and Roscoe B. White, Phys. Fluids **17**, 1211 (1974).
[33] J. Delettrez, R. Epstein, M. C. Richardson, P. A. Jaanimagi, and B. L. Henke, Phys. Rev. A **36**, 3926 (1987).
[34] R. C. Malone, R. L. McCrory, and R. L. Morse, Phys. Rev. Lett. **34**, 721 (1975).
[35] C. Stoeckl, V. Yu. Glebov, D. D. Meyerhofer, W. Seka, B. Yaakobi, R. P. J. Town, and J. D. Zuegel, Rev. Sci. Instrum. **72**, 1197 (2001).
[36] D. H. Froula, I. V. Igumenshchev, D. T. Michel, D. H. Edgell, R. Follett, V. Yu. Glebov, V. N. Goncharov, J. Kwiatkowski, F. J. Marshall, P. B. Radha, W. Seka, C. Sorce, S. Stagnitto, C. Stoeckl, and T. C. Sangster, Phys. Rev. Lett. **108**, 125003 (2012).
[37] I. V. Igumenshchev, D. H. Edgell, V. N. Goncharov, J. A. Delettrez, A. V. Maxomiv, J. F. Myatt, W. Seja, A. Shvydky, S. Skupsky, and C. Stoeckl, Phys. Plasmas **17**, 122708 (2010).
[38] R. K. Kirkwood, B. J. MacGowan, D. S. Montgomery, B. B. Afeyan, W. L. Kruer, J. D. Moody, K. G. Estabrook, C. A. Back, S. H. Glenzer, M. A. Blain, E. A. Williams, R. L. Berger, and B. F. Lasinski, Phys. Rev. Lett. **77**, 2706 (1996).
[39] J. C. Fernández, J. A. Cobble, B. H. Failor, D. F. DuBois, D. S. Montgomery, H. A. Rose, H. X. Vu, B. H. Wilde, M. D. Wilke, and R. E. Chrien, Phys. Rev. Lett. **77**, 2702 (1996).
[40] D. S. Montgomery, B. B. Afeyan, J. A. Cobble, J. C. Fernndez, M. D. Wilke, S. H. Glenzer, R. K. Kirkwood, B. J. MacGowan, J. D. Moody, E. L. Lindman, D. H. Munro, B. H. Wilde, H. A. Rose, D. F. Dubois, B. Bezzerides, and H. X. Vu, Phys. Plasmas **5**, 1973 (1998).
[41] R. A. Fonseca, L. O. Silva, F. S. Tsung, V. K. Decyk, W. Lu, C. Ren, W. B. Mori, S. Deng, S. Lee, T. Katsouleas, and J. C. Adam, in Computational Science - ICCS 2002, Lecture Notes in Computer Science Vol. 2331, Springer, Berlin, 2002, p. 342.
[42] R. Yan, C. Ren, J. Li, A. V. Maximov, W. B. Mori, Z.-M. Sheng, and F. S. Tsung, Phys. Rev. Lett. **108**, 175002 (2012).
[43] H. X. Vu, J. M.Wallace, and B. Bezzerides, Phys. Plasmas **1**, 3542 (1994).
[44] S. Depierreux, J. Fuchs, C. Labaune, A. Michard, H. A. Baldis, D. Pesme, S. Hüller, and G. Laval, Phys. Rev. Lett. **84**, 2869 (2000).